Inorganic Chemistry

Article

Cite This: *Inorg. Chem.* XXXX, XXX, XXX−XXX

pubs.acs.org/IC

Utilizing Charge Effects and Minimizing Intramolecular Proton Rearrangement to Improve the Overpotential of a Thiosemicarbazonato Zinc HER Catalyst

Steve P. Cronin,[†] Abdullah Al Mamun,[†] Megan J. Toda,[†] Mark S. Mashuta,[†] Yaroslav Losovyj,[‡] Pawel M. Kozlowski,[†] Robert M. Buchanan,[†] and Craig A. Grapperhaus*[,†]

[†]University of Louisville, Department of Chemistry, 2320 South Brook Street, Louisville, Kentucky 40292, United States

[‡]Department of Chemistry, Indiana University Bloomington, Bloomington, Indiana 47405, United States

Supporting Information

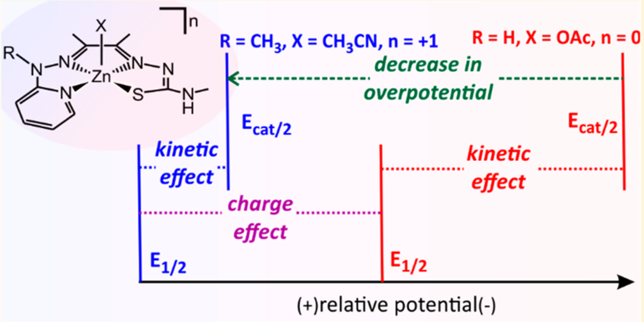

ABSTRACT: The zinc(II) complex of diacetyl-2-(4-methyl-3-thiosemicarbazone)-3-(2-hydrazonepyridine), ZnL^1 (**1**), was prepared and evaluated as a precatalyst for the hydrogen evolution reaction (HER) under homogeneous conditions in acetonitrile. Complex **1** is protonated on the noncoordinating nitrogen of the hydrazonepyridine moiety to yield the active catalyst Zn(HL^1)OAc (**2**) upon addition of acetic acid. Addition of methyl iodide to **1** yields the corresponding methylated derivative ZnL^{2}I (**3**). In solution, partial dissociation of the coordinated iodide yields the cationic derivative **3′**. Complexes **1**−**3** were characterized by ^{1}H NMR, FT-IR, and UV−visible spectroscopies. The solid-state structures of **2** and **3** were determined by single crystal X-ray diffraction. HER studies conducted in acetonitrile with acetic acid as the proton source yield a turnover frequency (TOF) of 7700 s^{-1} for solutions of **1** at an overpotential of 1.27 V and a TOF of 6700 s^{-1} for solutions of **3** at an overpotential of 0.56 V. For both complexes, the required potential for catalysis, $E_{cat/2}$, is larger than the thermodynamic reduction potential, $E_{1/2}$, indicative of a kinetic barrier attributed to intramolecular proton rearrangement. The effect is larger for solutions of **1** (+440 mV) than for solutions of **3** (+160 mV). Controlled potential coulometry studies were used to determine faradaic efficiencies of 71 and 89% for solutions of **1** and **3**, respectively. For both catalysts, extensive cycling of potential under catalytic conditions results in the deposition of a film on the glassy carbon electrode surface that is active as an HER catalyst. Analysis of the film of **3** by X-ray photoelectron spectroscopy indicates the complex remains intact upon deposition. A proposed ligand-centered HER mechanism with **1** as a precatalyst to **2** is supported computationally using density functional theory (DFT). All catalytic intermediates in the mechanism were structurally and energetically characterized with the DFT/B3LYP/6-311g(d,p) in solution phase using a polarizable continuum model (PCM). The thermodynamic feasibility of the mechanism is supported by calculation of equilibrium constants or reduction potentials for each proposed step.

INTRODUCTION

With increasing concern over climate change and the mounting demands for fuel, the need for renewable energy is ever present.[1−3] A part of the potential solution is the production of hydrogen from renewable and clean resources as an energy carrier. However, the hydrogen evolution reaction (HER) requires a catalyst to overcome the kinetic barrier. The most effective catalyst for HER is platinum; however, platinum is a precious metal and scarce resource. Of the multiple alternate catalysts explored, MoS$_2$ has received significant attention due to its high turnover frequency (TOF) at a relatively low overpotential. The activity of MoS$_2$ is proposed to occur on sulfur-edge sites without direct participation of the metal center in the bond-making/-breaking processes.[4−6] The importance of ligand participation in the coordination of substrate and evolution of H$_2$ is highlighted in the homogeneous systems developed by DuBois where a pendant amine acts as a proton shuttle to bring solution protons to the metal hydride active site.[7]

Traditionally, HER catalysis has proceeded through a metal hydride pathway: either through heterolytic M−H bond cleavage in a reaction with H$^+$ or homolytic M−H bond cleavage via coupling of two metal hydrides.[8] Recently, alternate ligand-centered pathways that do not involve a metal hydride have been reported. In 2015, Grapperhaus and co-workers developed a HER catalyst based on a coordinatively saturated Re(PS)$_3$ complex that was proposed to proceed via a ligand-centered route similar to MoS$_2$, although the possibility of a seven-coordinate rhenium hydride

Received: June 28, 2019

DOI: 10.1021/acs.inorgchem.9b01912
Inorg. Chem. XXXX, XXX, XXX−XXX

intermediate could not be excluded.[9] Shortly after, Berben and co-workers developed a $[(^{Ph}I_2P^{2-})Al(THF)Cl]$ complex that evolves hydrogen, exclusively from the ligand framework.[10] More recently, there has been significant interest in the application of metal bis-thiosemicarbazone (BTSC) complexes (Scheme 1) as HER catalysts with a redox-active ligand.[11−15]

Scheme 1. Comparison of BTSC Complexes with ZnL^1

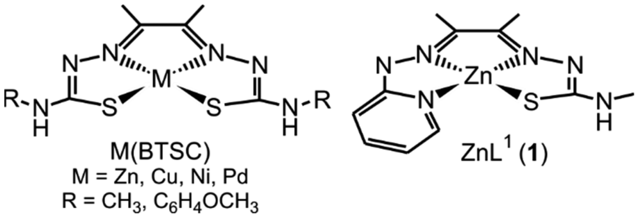

In all of the M(BTSC) HER catalysts investigated to date, the ligand is directly involved as a site of reduction and protonation. The exact mechanism is dependent on the identity of the metal. For Ni, the ligand assists the metal-centered hydrogen evolution activity.[13,14] In that case, the initial reduction and protonation occur on the BTSC ligand framework. Metal-centered reduction results in hydrogen migration yielding a metal hydride intermediate, which then reacts with a proton to yield H_2. A similar mechanism is reported for a related bis-dithiocarbazate nickel HER catalyst.[16] For Cu, the metal assists the ligand-centered activity.[12] The metal serves as an electron reservoir for ligand-centered H_2 evolution via coupling of hydrogens on adjacent nitrogen atoms in the ligand framework, without participation of a metal hydride. Interestingly, the Pd catalyst is proposed to follow a similar route, although reduction of the BTSC ligand occurs before protonation and the hydrogen evolution step happens directly from the ligand framework.[15] For Zn, all protonation and reduction events are ligand-centered.[11] Evolution of H_2 is proposed to occur via heterolytic N−H bond cleavage involving a dinuclear catalyst. Analysis of the spin density plot for the Zn(BTSC) complex shows the distribution of density is primarily on one of the TSC groups, suggesting ligands with a single TSC could be employed as HER catalysts.

In the current manuscript, we examine the HER activity of a previously reported Zn complex of diacetyl-2-(4-methyl-3-thiosemicarbazone)-3-(2-hydrazonepyridine) (H_2L^1). This ligand and its Cu and Zn complexes were first reported by Cowley and co-workers[17,18] and have been used as imaging agents. Structurally similar to BTSCs, it contains a pyridine donor in place of one of the TSC to form C_s symmetric metal complexes. The mononuclear Zn complex, ZnL^1 (**1**) and its $N_{hydrazino}$ methylated derivative ZnL^2I (**3**), are active HER catalysts operating with similar and substantial TOFs but at significantly different overpotentials.

RESULTS AND DISCUSSION

Scheme 2. Synthetic Routes for Compounds 1−3

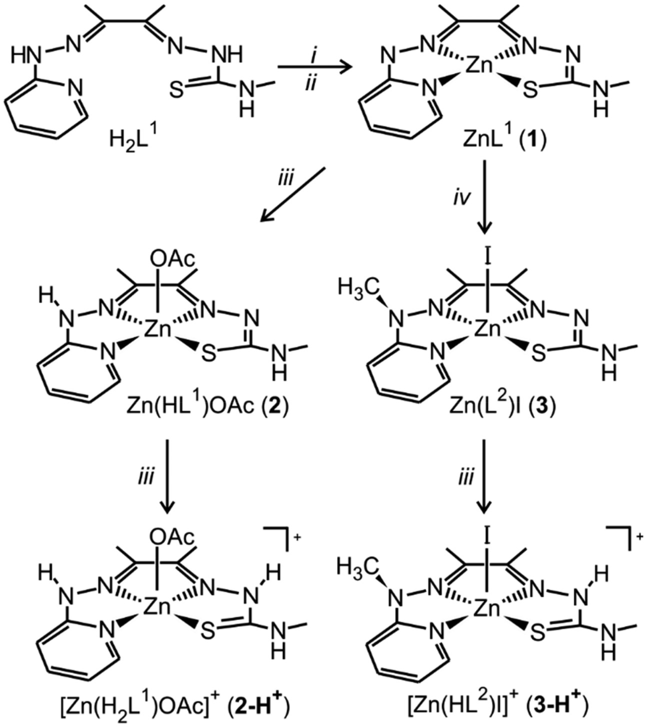

i = $Zn(OAc)_2$, EtOH; *ii* = NaOH, MeOH; *iii* = HOAc, MeOH; *iv* =MeI, acetonitrile

Synthesis and Characterization. The compounds $ZnL^1(CH_3OH)$ (**1**), $Zn(HL^1)OAc$ (**2**), and ZnL^2I (**3**) were prepared as shown in Scheme 2. The ligand H_2L^1 was prepared as previously reported by Cowley.[17] The single-crystal X-ray structure of **1**·CH_3OH has been published; however, no synthetic procedure for **1** was reported.[17] The synthesis of the related aqua complex $[ZnL^1H_2O]\cdot 2H_2O$ is known.[18] We prepared **1** by addition of zinc acetate to an ethanol solution of the H_2L^1 yielding a yellow precipitate following reflux. Addition of excess sodium hydroxide to the crude product in methanol allowed isolation of pure **1** as a dark orange solid upon workup. The ^1H and ^{13}C NMR of **1** is consistent with those reported for $[ZnL^1H_2O]\cdot 2H_2O$, including resonances for the coordinated methanol. The FT-IR of **1** is consistent with that of $[ZnL^1H_2O]\cdot 2H_2O$, with the exception that **1** shows a broad absorption peak at 3300 cm^{-1} characteristic of the methanol O−H stretch while $[ZnL^1H_2O]\cdot 2H_2O$ shows a broad water absorption peak near 3200 cm^{-1}. For **1**, a band at 1388 cm^{-1} assigned to the C−O−H stretch of methanol is also observed.

Protonation of **1** with acetic acid in methanol or acetonitrile resulted in a color change from orange to yellow associated with formation of **2**. The electronic spectrum of **1** in MeCN has a broad feature near 500 nm and sharp peaks at 324 and 274 nm, as in Figure 1A. Upon addition of acetic acid, the solution changes color from red-orange to yellow due to the loss of intensity of the 500 nm band. The new features of **2** grow in at 329 and 420 nm with isosbestic points at 295 and 360 nm consistent with protonation of the hydrazino-nitrogen.

The ^1H NMR spectrum for **2** in DMSO-d_6 displays a peak at 9.73 ppm that indicates protonation of the hydrazino pyridine moiety. Furthermore, a peak at 1.80 ppm indicates a coordinated acetate. Analysis of the region from 6.8 to 8.2 ppm shows five prominent signals: 6.80, 7.21, 7.23, 7.82, and 8.14 ppm corresponding to the protons on the pyridine moiety and the amine on the TSC. The FT-IR spectrum reveals an N−H stretch at 3360 cm^{-1} and three bands at 3241, 2935, and 1640 cm^{-1} assigned to the coordinated acetate.

The UV−visible spectrum of **2** in acetonitrile shows two bands at 329 and 420 nm, as in Figure 1B. Upon addition of

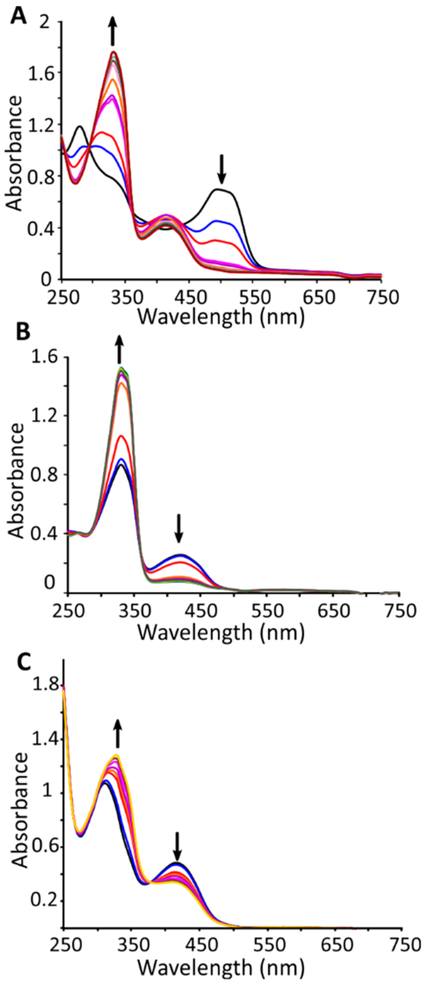

Figure 1. UV/visible spectra in acetonitrile (path length = 1 cm) of (A) 0.1 mM of **1** titrated with 0.01 M acetic acid from 0.1 to 1 equiv, (B) 0.1 mM **2** titrated with 0.1 M acetic acid from 2 to 16 equiv, and (C) 0.1 mM of **3** titrated with 0.1 M acetic acid from 2 to 16 equiv.

acid, the peak at 420 nm decreases in intensity, and the band at 329 nm increases with an isosbestic point at 360 nm. To confirm the identity of new species as **2-H**$^+$, crystals of **2** were dissolved in DMSO-d_6, and HPF_6 was added. Analysis via ^{1}H NMR showed two new peaks at 11.54 and 10.30 ppm, each integrating to 0.37 H with respect to the hydrazino nitrogen, attributed to two forms of **2-H**$^+$ in equilibrium. One protonation site is assigned as the neighboring imido on the pyridine side and the other to the opposite hydrazino nitrogen on the thiosemicarbazone side.

Compound **3** was prepared as an air-stable brown/yellow solid by methylation of **1** in MeCN upon reflux. The ^{1}H NMR spectrum in DMSO shows a resonance at 3.62 ppm assigned to the $N-CH_3$ protons in addition to the backbone methyl resonances at 2.07 and 2.33 ppm, and the peak at 2.90 ppm is the TSC methyl resonance. The region from 7.2−8.1 ppm contains a single set of peaks at 7.16, 7.38, 8.04, and 8.10 ppm assigned to the pyridine moiety and a broad singlet at 7.86 ppm for the NH of the pendant amine of the TSC. The FT-IR spectrum of **3** revels a broad peak at 1080 cm^{-1} and a shift in a peak at 1219 cm^{-1} from 1214 cm^{-1}. These are indicative of changes in the C=N in the imines of the backbone.

The UV/vis spectrum of **3** in MeCN includes two bands at 304 and 420 nm, as in Figure 1C. Upon addition of acid, the band at 304 nm increases along with a decrease in intensity of the band at 420 nm. This results in an isosbestic point at 380 nm. To further probe the identity of **3-H**$^+$, complex **3** was dissolved in DMSO-d_6 and an excess of HPF_6 was added. The ^{1}H NMR spectrum clearly demonstrates new features at 11.54, 10.53, and 10.24 ppm consistent with protonation at the coordinated amido nitrogens and the hydrazino nitrogen. The integration of all three new peaks is approximately $^1/_3$ of a proton each with respect to the backbone methyl integration indicating tautomerization over the three sites.

Structural Determination. Slow evaporation of a methanol solution of **1** yielded triclinic crystals with unit cell parameters consistent with those of the previously reported **1** structure. Single crystals of **2** and **3** were obtained upon slow evaporation of an acetonitrile/methanol/acetone mixture (1:1:1). Crystal data and structure refinement details for **2** and **3** are listed in Table S7. A comparison of selected metric parameters for **1**−**3** and the related complex $[Zn(HL^1)H_2O]NO_3$ (**2′**)[18] is provided in Table 1.

ORTEP representations[19] of **2** and **3** are provided in Figure 2. Each complex contains Zn in a square pyramidal environment with the metal sitting slightly above the basal plane defined by the N_3S donor atoms of the L^1 chelate. The axial position is occupied by acetate in **2** and iodide in **3**. The protonated hydrazino N in **2** is best described as trigonal planar with a $C-N_{ImPyr}-N_{HyPyr}-H$ torsion angle of 14°, which

Table 1. Selected Bond Distances (Å), Bond Angles (deg), and Torsion Angles (deg)[a]

	1[17]	**2**	**2′**[18]	**3**
$Zn-N_{ImTSC}$	2.106(2)	2.1511(18)	2.0985(19)	2.098(3)
$Zn-N_{Pyr}$	2.057(2)	2.1245(18)	2.082(2)	2.110(3)
$Zn-N_{ImPyr}$	2.098(2)	2.138(17)	2.109(2)	2.142(2)
$Zn-S1$	2.3279(7)	2.3113(6)	2.324(7)	2.3375(8)
$C-N_{HyPyr}$	1.376(3)	1.382(3)	1.385(3)	1.398(4)
$N_{ImPyr}-N_{HyPyr}$	1.361(3)	1.355(2)	1.345(3)	1.366(3)
$Zn-X$	2.0443(19)	1.9868(15)	1.9974(18)	2.6235(4)
$N_{Pyr}-Zn-S1$	118.99(1)	117.82(5)	118.93(1)	112.88(8)
$N_{ImPyr}-Zn-X$	97.55(1)	95.11(6)	98.76(1)	96.89(7)
$N_{ImPyr}-Zn-S1$	150.27(1)	137.61(5)	150.65(1)	145.65(7)
$N_{Pyr}-Zn-N_{ImTSC}$	147.19(1)	144.68(1)	145.49(1)	137.78(10)
$C-N_{ImPyr}-N_{HyPyr}-R$		14	7	43.18

[a] X = O in **1**, **2**, and **2′** and I in **3**; R = H in **2** and **2′** and CH_3 in **3**. Nitrogen atoms are labeled according to type where $N_{ImTSC} = N_1$, $N_{Pyr} = N_5$, $N_{ImPyr} = N_3$, and $N_{HyPyr} = N_4$ in Figure 2. The carbon atom C refers to the backbone carbon C3 in Figure 2.

DOI: 10.1021/acs.inorgchem.9b01912
Inorg. Chem. XXXX, XXX, XXX−XXX

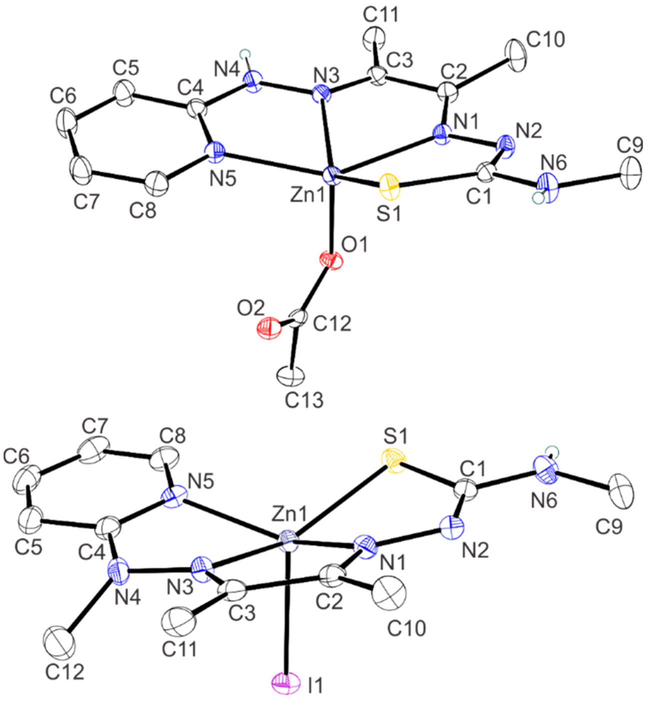

Figure 2. ORTEP[19] representations of **2** (top) and **3** (bottom).

is similar to that in **2′**, 6.7°. In contrast, the methylated hydrazino N in **3** is distorted toward pyramidal as evidenced by the C$-$N$_{\mathrm{ImPyr}}$$-N_{\mathrm{HyPyr}}$$-CH_3$ torsion angle of 43°. This is attributed to steric interactions between the hydrazino-N and backbone methyl groups. The metal−ligand bond distances in **2** and **3** are similar to those in **1** and **2′** (Table 1). Differences in the Zn−N$_{\mathrm{Pyr}}$ and Zn−N$_{\mathrm{ImPyr}}$ bond distances between the complexes are attributed to electronic effects associated with modification of the nearby hydrazino N environments and coordination of anions in the axial position.

Electrochemical Characterization. The cyclic voltammogram (CV) of **1** in acetonitrile, shown in Figure 3 in black, displays an irreversible one-electron reduction at −2.47 V and an irreversible one-electron oxidation at −0.36 V. Scans of only the anodic region confirm the one-electron oxidation is not coupled to the one-electron reduction (Figure S14). All reported potentials listed are referenced to the Fc$^+$/Fc couple ($E_{1/2}$ = 0.48 V vs Ag/Ag$^+$). The reduction event at −2.47 V is slightly more cathodic than that of ZnATSM, which occurs at −2.15 V in acetonitrile.[11] The CV of **2** in acetonitrile shows three one-electron reduction events at −2.23, −2.46, and −2.87 V and a one-electron oxidation event at −0.17 V (Figure 3, blue trace). The reduction event at −2.23 V is assigned to the **2**/**2**$^-$ redox couple, which is shifted by +0.23 V with respect to **1**/**1**$^-$. Reduction of **2** to **2**$^-$ increases the basicity of the ligand resulting in proton transfer near the electrode to generate a mixture of **1**, **2**, and **2-H**. This process facilitates the peak at −2.46 V, which is at the same potential of that of **1**/**1**$^-$. The final reduction event at −2.87 V is attributed to generation of a small amount of H$_2$. Furthermore, the oxidation peak is likely associated with the **2**/**2**$^-$ couple as no peak exists if an anodic scan is completed (Figure S14). The CV of **3** in acetonitrile shows two irreversible reduction events at −1.79 and −2.02 V and three irreversible oxidation events at −0.19, 0.06, and 0.38 V (Figure 3, red trace). The more cathodic reduction is assigned to the **3**/**3**$^-$ couple, for which the iodide remains coordinated to the metal center. The event at −1.79 V is attributed to reduction of **3′**, which results from dissociation of iodide from Zn in solution. The oxidation event at 0.38 V is attributed the oxidation I$^-$ to I$_2$.[20] All oxidations are observed when only the anodic region is scanned (Figure S14).

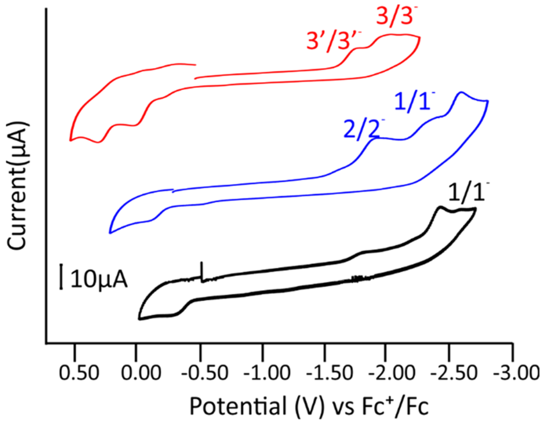

Figure 3. CVs of 1.0 mM **1** (black), **2** (blue), and **3** (red) in acetonitrile containing 0.1 M Bu$_4$NPF$_6$ as supporting electrolyte. Data were recorded at a scan rate of 0.2 V/s.

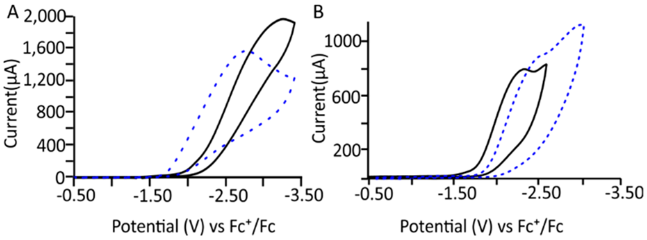

Figure 4. CVs recorded in acetonitrile at a scan rate of 0.2 V/s in 0.1 M Bu$_4$NPF$_6$: (A) The blue dashed line is the background scan of 0.240 M acetic acid with no catalyst. The solid black line is the scan of **1** in the presence of 0.240 M acetic acid with the background scan of 0.240 M acetic acid subtracted. (B) The blue dashed line is the background scan of 0.072 M acetic acid with no catalyst. The solid black line is the scan of **3** in the presence of 0.072 M acetic acid with the background scan of 0.072 M acetic acid subtracted.

Homogeneous Catalytic Hydrogen Evolution: Cyclic Voltammetry. Addition of acetic acid to a 1 mM solution of **1** in acetonitrile exhibits a catalytic wave at −3.29 V (Figure 4A). The current is significantly higher than the background reduction of acetic acid at the glassy carbon electrode. At lower acid concentrations, a prepeak attributed to **2-H**$^+$ is observed at −1.81 V that shifts to −1.74 V under successively more acidic conditions. Under saturating acid conditions, this peak is hidden by the catalytic wave. On the basis of the background-corrected current under saturating conditions, the estimated TOF is calculated as 7700 s^{-1}. The overpotential was calculated as 1.27 V from the $E_{\mathrm{cat}/2}$ value of −2.67 V using the method of Artero and co-workers.[21] The reaction is first-order in **1** and second-order in acid. At high acid concentrations, it is clear that some side phenomena likely occurs as the CV appears not to be under diffusion control (Figure S15). The most common of these are "consumption of the substrate, deactivation of the catalyst, and inhibition by products".[22] We attribute the nonideal behavior to consumption of the substrate at the electrode as this process is undergoing catalysis; however, it is also possible that this is evidence for a buildup of an electroactive film. Since acetic acid in acetonitrile can sometimes give "false" second-order plots,[23] catalytic experiments were repeated with phenol (Figure S18). These experiments confirmed the reaction is second-order with respect to acid (Figure S19 and S20). Kinetic isotope studies done using acetic acid-d_1 (CH_3OOD) yielded a KIE of 1.66 ± 0.15 (Figure S24 and S25). The KIE is similar to that reported for Zn-ATSM, which is proposed to proceed via a ligand hydride mechanism with attack by the hydride on a proton in solution or bound to ligand/metal framework.[11] Further studies using the exceedingly weak acid methanol show no catalysis, indicating that methanol is not strong enough to doubly protonate the complex **1** (Figure S21).

Addition of acetic acid to a 1 mM acetonitrile solution of **3** yielded a catalytic wave with peak current at −2.15 V and an onset potential of −1.49 V. A prepeak is observed at −1.81 V under low acid concentrations (<0.030 M). The prepeak is indicative of protonation of **3** to generate **3-H**$^+$. At acid concentrations of >0.030 M, the prepeak is obscured by the catalytic wave. Notably, at acid concentrations of >0.072 M the catalyst becomes inactivated. On the basis of the current under scan-rate-independent conditions in 0.072 M acetic acid solution, the TOF is calculated as 6700 s^{-1} at an overpotential of −0.56 V with $E_{cat/2} = -1.95$ V (Figure 4B). The catalytic current shows a second-order dependence with respect to acid and a first-order dependence with respect to catalyst. Kinetic isotope studies with deuterated acetic acid resulted in a KIE of 1.30 ± 0.23 similar to **1**.

Controlled Potential Coulometry. To quantify gas production and determine faradic efficiency, controlled potential coulometry (CPC) was conducted in acetonitrile at an applied potential of −2.60 V for **1** and −1.80 V for **3** (vs Ag/AgCl) (Figure 5). A sample of the headspace gas by gas chromatography confirmed the product as hydrogen. Compound **1** generated 6.89 mL of gas over a 2 h period. Control experiments in the absence of **1** at this potential yielded 2.26 mL over the same time period. On the basis of a total volume of hydrogen generated by the catalyst of 4.63 mL, this corresponds to a TON of 189 in 2 h and a faradaic efficiency of 71%. For **3**, the total volume of gas produced, after correcting background reactivity, was 0.20 mL associated with a TON of 8.4 and a faradaic efficiency of 89%. Data for these experiments is tabulated in Table S5. The relatively low TONs as compared to the TOFs results from the fact that only catalyst at the electrode surface actively generates hydrogen, but the bulk concentration of the catalyst is used to calculate the TON values.

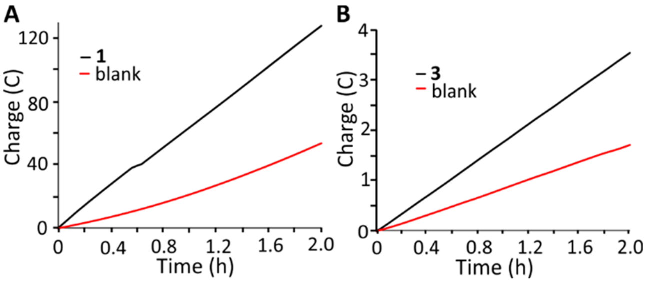

Figure 5. CPC for 2 h for **1** at an applied potential of −2.60 V vs Ag/AgCl (A) and **3** at an applied potential of −1.80 V vs Ag/AgCl (B).

Control Experiments. *Soak Test.* To determine if complexes chemically adsorb to the glassy carbon electrode, a soak test was performed for both **1** and **3**. The electrode was placed in a solution containing catalyst, substrate, solvent, and supporting electrolyte overnight. The electrode was removed from the solution, rinsed, and placed into a fresh solution of electrolyte. For both **1** and **3**, no peaks were observed, even upon addition of substrate, indicating that no significant quantities of catalyst chemically adsorbed on to the electrode under these conditions.

Post-CV Dip Test. To determine if catalysts adsorb to the electrode under electrocatalytic conditions, a post CV dip test was performed for both **1** and **3**. CV data were collected under acid-saturating electrocatalytic conditions. The glassy carbon electrode was removed, rinsed, and placed into a fresh solution of electrolyte, and the CV was recorded. For **1**, after 10 cycles the electrode showed no significant peaks when placed in a fresh solution, even upon addition of 0.240 M acetic acid (Figures S36−S38). However, when the test was repeated using 30 cycles, a peak at −2.65 V was observed upon placing the electrode in fresh electrolyte suggesting that some of **1** had adsorbed on the electrode (Figures S39−S40). Addition of acid confirmed that the adsorbed species was catalytically active for HER (Figure S41). For **3**, after 10 cycles under acid-saturated conditions, the electrode showed small peaks at −1.72 and −2.04 V when placed in a fresh solution of electrolyte consistent with adsorption of **3** (Figure S47). Upon addition of acid, electrocatalytic HER is observed. These results indicated that upon prolonged cycling a significant amount of HER activity is likely due to absorbed catalyst. However, since initial cycles show catalytic activity that cannot be attributed to adsorbed complex, both **1** and **3** are considered competent homogeneous HER catalysts.

Postelectrolysis Dip Test. To further investigate the adsorption of catalyst on the electrode during prolonged electrocatalytic activity, bulk electrolysis was performed in acetonitrile with 0.240 or 0.072 M acetic acid for **1** and **3** at applied potentials of −3.10 and −2.30 V, respectively. As in the other control experiments, the electrode was then rinsed and placed in a fresh solution of electrolyte, and CV data was collected. As described below, the results confirm the adsorption of both **1** and **3** as catalytically active films on glassy carbon.

For **1**, postelectrolysis CV of the glassy carbon electrode showed reduction events at −0.60 and −2.10 V in the absence of acid. Additionally, an oxidation occurs at −0.10 V that is substantially larger in current in comparison to the reduction events attributed to desorption of complex from the electrode's surface. When 0.240 M acetic acid is added to this solution, a prepeak is observed at −1.10 V along with a catalytic peak at −2.10 V. Notably, the catalytic peak for HER is shifted by 1.2 V relative to the homogeneous solution value of −3.29 V. A similar shift of ∼1.2 V was observed for the HER activity of Cu(ATSM) upon adsorption on glassy carbon.[12] Recently, we also reported significant anodic shifts in HER overpotential for planar Ni(ATSM) derivatives adsorbed on glassy carbon upon conditioning of the electrode through repeated cycling.[24] That study concluded that translation of a homogeneous catalyst to an electrode without covalent tethering depends on the physical structure of the catalyst as it "relates to catalyst−electrode interactions and charge transfer between electrode, catalyst, and substrate". To confirm the identity of the adsorbed species deposited during bulk electrolysis of **1**, the film was removed from the electrode surface and analyzed by XPS.

For **3**, the catalyst was subjected to a bulk electrolysis over 24 h at an applied potential of −2.30 V. After controlled potential electrolysis, the electrode was rinsed with DI H_2O and placed into a fresh electrolyte solution and the CV was scanned between −2.40 and 0.60 V. Two reduction events were observed at −1.30 and −1.90 V along with two oxidation events at −0.30 and 0.10 V, implying an electroactive compound is deposited on the electrode surface during electrolysis. The film is catalytically active for HER with a peak current of 690 μA at −2.05 V under acid-saturating conditions. This is similar to the catalytic activity observed for the film of **3** deposited during the post-CV dip test.

XPS Film Analysis. To identify the composition of the catalytically active films deposited during the control experiments, the electrolysis conditions for the postelectrolysis dip test were repeated, and the coating on the electrode surface was analyzed by XPS (see the Supporting Information). For **1**, the coating showed atomic percentages for N/Zn/S in an approximately 6:1:1 ratio consistent with the parent compound. Furthermore, the XPS showed two peaks for nitrogen consistent with the intact complex having sp^2- and a sp^3-hybridized nitrogen. The carbon percentage in the coating could not be determined due the large signal from the glassy carbon electrode and/or adventitious carbon. Films of **3** showed a N/Zn ratio of 6:1 with a variable amount of S (0.3−0.5 equiv) and less than 0.1 equiv of iodide. Since XPS is extremely surface-sensitive, the variability and low quantity of S could indicate that not all of the sulfurs are on the surface of the absorbed species. The marginal amount of iodide indicates the film contains cation **3′** (iodide-dissociated) that is charge-balanced by PF_6^-. Furthermore, XPS elemental mapping shows that the N 1s and Zn 2p elemental maps overlap. The mapping, along with the consistent 6:1 N/Zn ratio, indicates the complex is likely still intact despite the low sulfur concentrations. However, we cannot exclude the possibility that some ligand degradation of **3** occurs. Since a Pt counter electrode was used during electrolysis, the films were analyzed for Pt, and none was observed.

Postelectrolysis Rinse Test. Since the postelectrolysis dip test produced an electrocatalytically active film over a prolonged time frame (24 h), a postelectrolysis rinse test was conducted over a shorter time frame (2 h) for comparison with the CPC experiments. In a typical experiment, an acetonitrile solution of **1** containing 0.1 M NBu_4PF_6 and 0.240 M acetic acid was subjected to CPC for 2 h. The electrodes were then removed and rinsed with DI H_2O. The electrodes were then placed into a clean cell containing 0.1 M NBu_4PF_6 and 0.240 M acetic acid but no catalyst. A second 2 h cycle of CPC was then completed. Similar experiments were conducted for **3**. For both complexes **1** and **3**, an appreciable charge was produced in the initial CPC cycle, but after rinsing the electrode, no significant charge above the acid-blank experiment was observed (Figures S54 and S55). This indicates that an electrocatalytically active film is not generated over the time frame of the 2 h CPC experiments. All catalysis under these conditions is attributed to homogeneous catalysis and not heterogeneous catalysis.

Density Functional Theory Investigation. To explore the mechanism of the H_2 evolution a series of density functional theory (DFT) calculations were performed on **1** (S = 0, q = 0) and its protonated and reduced derivatives **2** (S = 0, q = 0), **2-H**$^+$(S = 0, q = +1), **2-H** (S = 1/2, q = 0), **2-H**$_2^+$ (S = 1/2, q = +1), and **2-H**$_2$ (S = 0, q = 0). The initial structural parameters for the calculations were taken from crystal structure data. The model structures were then optimized with DFT using the B3LYP functional and 6-311g(d,p) basis set.[25,26] This level of theory has been shown to be reliable for similar complexes.[13] The calculations were carried out in solvent employing a polarizable continuum model (PCM) using acetonitrile as a solvent.[27] The thermodynamic feasibility of the interconversion of complexes through protonation or reduction steps was evaluated by the calculation of equilibrium constant (K) for chemical steps or reduction potential ($E_{1/2}$) for reduction steps. The thermodynamic parameter K was calculated by optimizing products and reactants and utilizing both acetic acid and acetate ions as independent calculations. The thermodynamic parameter $E_{1/2}$ was calculated by using both a direct reference to ferrocene and a Born−Haber cycle.[28,29] A summary of the calculations and a comparison of calculated vs experimental reduction potentials can be found in the sample calculations and Table S6. It should be noted that the calculated K values are lower estimates as outersphere interactions between the metal-containing cation and acetate counterion, which could stabilize the products, were not included.

The initial optimized structural model of **1** was in good agreement with the crystal structure. The optimized structure is square planar with Zn−S and Zn−N bond distances within 0.1 Å of the experimentally determined values. To verify the location of the additional proton in **2**, the optimized structure of **1** was modified by addition of an acetate at the Zn center and addition of a proton at all possible protonation sites of the ligand. Geometry optimizations were conducted for all the possible structures. Frequency calculations were also conducted after geometry optimizations to confirm that the optimized structure corresponds to a true minimum. Protonation at the hydrazino nitrogen N_4 was found to be energetically most stable (Figure 6A). The next lowest energy structure, with protonation at the opposite hydrazino nitrogen N2, was 7.6 kcal/mol higher. The calculated K for the

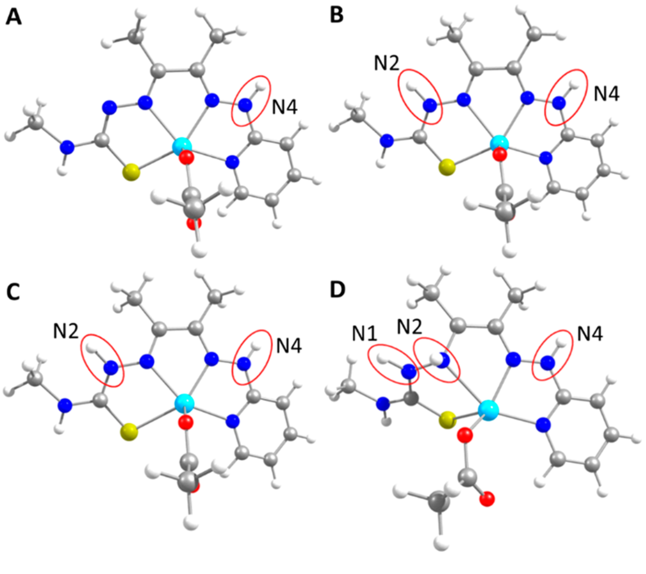

Figure 6. Lowest energy optimized structures with protonation sites circled in red for (A) **2**, (B) **2-H**$^+$, (C) **2-H**, and (D) **2-H**$_2^+$.

protonation of **1** to **2** is 214, indicating the step is thermodynamically favorable.

Next, the protonation of **2** to **2-H**$^+$ was evaluated by addition of a proton to the lowest energy structures of **2**. Structures were then optimized and the stationery points were confirmed by frequency calculations. Protonation at the opposite hydrazino nitrogen N2 was energetically most stable (Figure 6B), whereas protonation on sulfur was 8.0 kcal/mol energetically less favorable. Protonation at other nitrogen sites are 10.6 kcal/mol or higher in energy. The calculated K for the protonation of **2** to **2-H**$^+$ is 9.2×10^{-3}. While this step is not as favorable as **1** to **2**, under acid-saturating conditions (240 mM), **2-H**$^+$ should be the only component in solution.

To evaluate the initial reduction event, the possible structures of **2-H**$^+$ were re-evaluated as neutral spin doublets and optimized with the same level of theory. The structure with protons at both N2 and N4 remains the lowest energy structure for **2-H** (Figure 6C). However, a tautomer with protons at the adjacent imido and hydrazino nitrogens N1 and N2 is only 1.6 kcal/mol higher in energy. The spin density distribution of the lowest energy structure shows delocalization over the ligand backbone. The calculated reduction potential for **2-H**$^+$ to **2-H** of −1.82 V is in good agreement with the experimental reduction potential of −1.97 V.

On the basis of the experimental observation that HER with **2** is second-order in acid, we next evaluated the addition of another proton to the lowest energy structures of **2-H** to yield the cationic spin doublet **2-H$_2$**$^+$ (Figure 6D). The possible protonation combinations were then optimized with frequency calculations. The most favorable of all the optimized structures has protons at N1, N2, and N4 (Figure 6D). The next lowest energy structure is 5.3 kcal/mol higher in energy with protons on N2, N4, and N5. The calculated K for the protonation of **2-H** to **2-H$_2$**$^+$ was found to be 56, indicating that this is a thermodynamically competent route under acid-saturating conditions.

Since the protonation of **2-H** to **2-H$_2$**$^+$ is thermodynamically favorable, we further evaluated its potential role in HER. Addition of an electron to **2-H$_2$**$^+$ yields the proposed hydrogen evolving complex, **2-H$_2$**. Three viable structures are located within 4.6 kcal/mol of each other (Figure 7). Interestingly, the lowest energy structure is distorted toward trigonal bipyramidal with protons at N1, N3, and N4. The H−N3−N4−H torsion angle is 48.2°. The next lowest energy structure (+1.4 kcal/mol) is tetrahedral with protons at N2, N3, and N4 with a H−N3−N4−H torsion angle of 96.6°. The final optimized structure is a distorted square pyramid with protons at N1, N2, and N4 is 4.6 kcal/mol above the minimum. The H−N1−N2−H torsion angle is 54.7°. The calculated reduction potential was found to be between −1.1 and −1.3 V indicating that reduction of **2-H$_2$**$^+$ is much easier than reduction of **2-H**. This can be seen in the CV under acid-saturating conditions, as under acid saturation the prepeak associated with reduction of **2-H** is obscured by the catalytic current. On the basis of these calculations, it cannot be determined which of these species, or combination of species, contributes to H_2 evolution.

The analogous methylated species was calculated as monocation **3-H$_2$**$^+$ with no coordinated acetate. In the absence of coordinated acetate, the complex adopts a tetrahedral-like environment. The likely hydrogen-evolving N1,N2-protonated species was lowest in energy. However, other tautomers are within 3.3 kcal/mol. The coordination of acetate is proposed to occur under high concentrations of acid corresponding with the loss of HER activity.

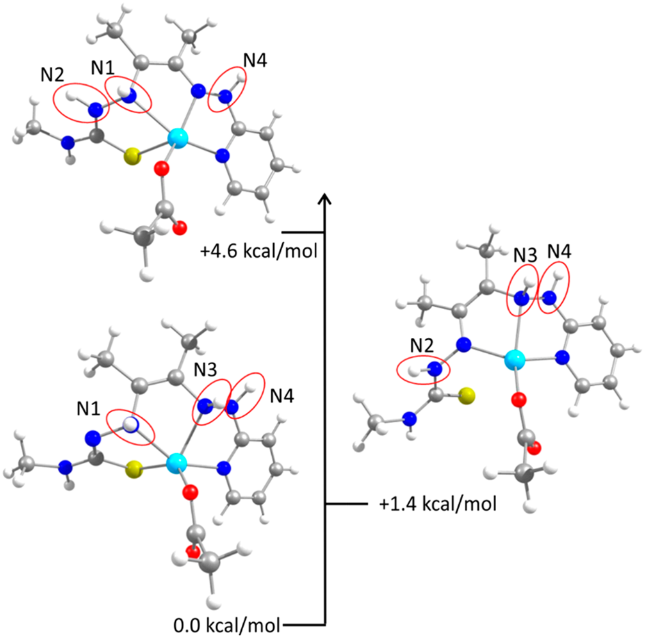

Figure 7. Three lowest energy optimized structures of **2-H$_2$** with protonation sites circled in red.

An alternate HER pathway for **2**, which does not require protonation to **2-H$_2$**$^+$, was also considered. This route presumes H_2 release upon direct reduction of the low lying HN1−N2H tautomer of **2-H**. The calculated reduction potential for **2-H**, −2.47 V, is accessible at $E_{cat/2}$ value of −2.67 V, and this route cannot be excluded. This route is not available for **3** due to the methylation of the hydrazino nitrogen N2.

Proposed HER Mechanism. A proposed HER mechanism based on experimental data during which the complexes are in homogeneous solution and computational results is shown in Scheme 3. Compound **1** serves as a precatalyst that is protonated to yield the active catalyst **2**. Complex **2** evolves hydrogen via a CECE mechanism in which C represents a chemical step (protonation) and E is an electrochemical step (reduction). Ligand-centered protonation of **2** to **2-H**$^+$ is followed by ligand-centered reduction to yield **2-H**. The second protonation step of the cycle yields **2-H$_2$**$^+$. The final reduction yields hydrogen-evolving complex **2-H$_2$** for which three energetically plausible structures were identified computationally. Our proposed mechanism prefers the distorted square pyramidal structure as it yields the lowest energy structure of **2** upon H_2 evolution (Scheme 3). The proposed mechanism for **3** is an analogous CECE pathway in which the proton on N4 in **2** is substituted with a methyl group, and no coordination of the acetate ligand occurs.

■ CONCLUSIONS

In the current study, we show that the HER activity previously reported for the related BTSC complex Zn(ATSM) is retained upon substitution of one thiosemicarbazone with a pyridyl functional group in **2** and **3** allowing for further expansion and refinement of this class of noninnocent ligands for HER. Re-evaluation of the TOF for Zn(ATSM) using the equation TOF $= 1.94\nu(i_c/i_p)^2$ gives a value of 4000 s^{-1} for Zn(ATSM) at an

Scheme 3. Proposed HER Mechanism

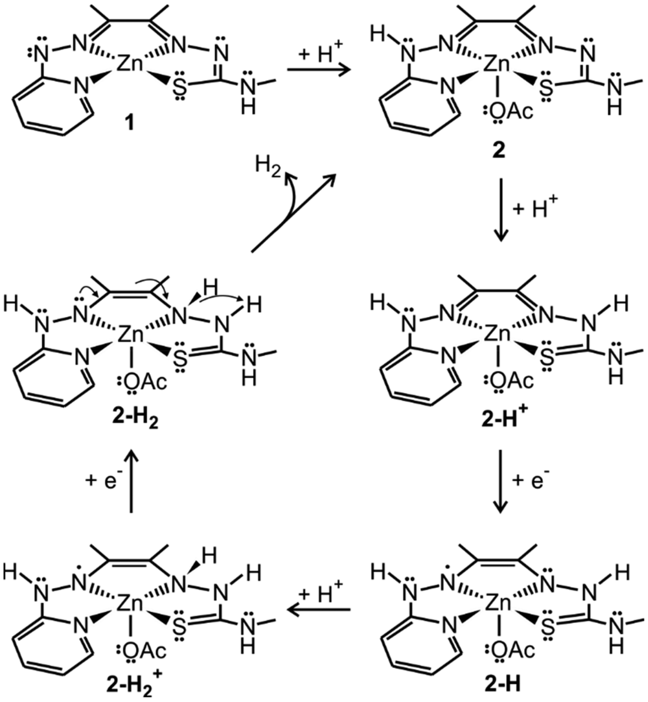

overpotential of 1.04 V. Catalysts **2** and **3** yield a TOF of ~7000 s^{-1} at scan-rate-independent conditions. Catalysts **2** and **3** are competent for HER under homogeneous conditions. Films containing **2** and **3** are observed after prolonged conditions, such as 30 continuous CV cycles without stirring or CPC beyond 2 h. However, under the conditions used to determine TOF and overpotential, contributions from deposited catalysts are not detectable.

Under homogeneous conditions, protonated complex **2** requires a significantly larger overpotential, 1.27 V, than does methylated complex **3**, 0.56 V, to achieve similar TOFs. The 710 mV shift in overpotential is attributed to a combination of two factors, see Figure 8. The first is a charge effect (*a*) accounting for a 440 mV shift in overpotential. Whereas **2** is neutral in solution with a coordinated acetate, the weakly coordinating iodide of **3** dissociates in solution to generate monocationic species **3′**. As a result, $E_{1/2}$ for cationic **3′** is 440 more accessible than the $E_{1/2}$ for **2**. This accounts for a majority of the 710 mV difference in overpotential for the two catalysts. A similar shift was seen by Rochford and co-workers where a protonation first pathway reduced the reduction potential by 450 mV.[30]

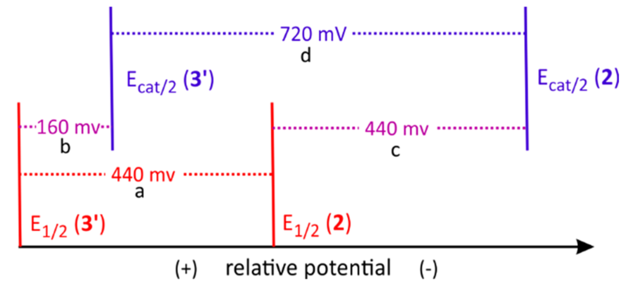

Figure 8. Relative values of $E_{1/2}$ and $E_{cat/2}$ for **2** and **3′**. The difference in $E_{1/2}$ values (*a*) reflects the difference in charge of the two catalysts. The difference between $E_{cat/2}$ and $E_{1/2}$ for each catalyst (*b* and *c*) represents the kinetic barrier due to intramolecular proton rearrangement in that catalyst. The difference in overpotential is determined by the difference in $E_{cat/2}$ (*d*), which equals $a + c - b$.

The remaining difference in overpotential of ~270 mV is attributed to differences in the rate of intramolecular proton transfer. As noted by Nocera and co-workers, catalysts operating via intermolecular proton transfer typically show $E_{cat/2}$ values near the thermodynamic $E_{1/2}$ value of the catalyst, while intramolecular proton transfer shifts $E_{cat/2}$ to more negative reduction potentials dependent on the scan rate.[31,32] As shown in Figure 8, the difference between $E_{cat/2}$ and $E_{1/2}$ is larger for **2** (440 mV) than that for **3′** (160 mV) indicating a larger kinetic barrier to intramolecular proton transfer in the former. Whereas hydrogen-evolving complex **2-H$_2$** has three energetically accessible tautomers (Figure 7), only one tautomer is possible in **3′** derivative due to methylation at the N4 site. The 280 mV difference in these kinetic values accounts for the remaining ~270 mV difference in overpotential.

Overall, the ~710 mV difference in overpotential for **2** and **3′** results from a combination of charge effects, ~440 mV, and kinetic effects, ~280 mV. The results demonstrate the utility of ligand design to combine factors to substantially lower overpotential. Furthermore, the HER activity of **2** and **3′** demonstrates the flexibility of the thiosemicarbazone framework as a platform for noninnocent ligand-derived electrocatalysts.

EXPERIMENTAL SECTION

General Synthetic Considerations. Unless otherwise specified, all precursory chemicals were purchased from TCI chemicals. All synthetic procedures were performed using clean and vacuum flame-dried glassware. All NMRs were completed on a Bruker 400-MHz NMR. All FT-IR experiments were completed on Perkins Elmer spectrum 100 with a diamond tip, as a powder or crystal. All UV/vis measurements were completed on a Variant Cary 50 Bio with fast scan capabilities. All solvents were purified with a solvent purification system made by MBraun.

Synthesis of ZnL^1 (1). H_2L^1 and all relevant precursors were made following previous published methods with some modifications.[18] Zinc acetate dihydrate (0.225 g, 1.23 mmol) was added to H_2L^1 (0.245 g, 0.927 mmol) in 30 mL of ethanol. This mixture was refluxed under N_2 for 16 h. The resulting solid was filtered and rinsed with cold ethanol and diethyl ether (85% yield). The isolated solid was found to contain a 6% impurity of **2** via ^{1}H NMR. To remove **2**, the solid was dissolved in methanol containing a 6-fold excess of NaOH, and the mixture was stirred for 5 days. The solution was the removed under vacuum, and the resulting solid was dissolved in ethanol and cooled to 0 °C for 24 h. The solution was filtered under vacuum, and the solid was discarded. The filtrate was removed under vacuum and dissolved in a minimal amount of methanol (2 mL) and layered with 30 mL of diethyl ether. An orange/red solid was isolated by vacuum filtration and rinsed with diethyl ether. Isolated yield was 0.182 g (0.556 mmol, 60%). The ^{1}H and ^{13}C NMR spectra of the solid are in good agreement with previously reported spectra of ZnL^1.[18]

Synthesis of Zn(HL^1)OAc (2). Complex **1** (10 mg, 0.00258 mmol) was dissolved in 10 mL of a 1:1:1 mixture of methanol/acetonitrile/acetone. To this were added 10 drops of glacial acetic acid (17.4 M) resulting in a color change from orange to yellow. Complex **2** was isolated as X-ray quality yellow crystals upon slow evaporation over several days at room temperature. Yield: 8.4 mg (0.00217 mmol), 83.7%. Anal. Calcd for $ZnC_{13}H_{18}N_6O_2S$: C, 40.30; H, 4.70%; N, 21.70. Found: C, 40.80; H, 4.78; N, 21.27. (+)ESI-MS, Mass Spec: *m*/*z* = 375, 381, 391, 397. ^{1}H NMR (400 MHz, DMSO-*d*$_6$) δ/ppm: 9.73 (N–N*H*), 8.14 (Ar–H), 7.82(N*H*–CH$_3$), 7.67(Ar–

H), 7.23(Ar−H), 6.80 (Ar−H), 2.82(NH−CH_3), 2.19(C−CH_3), 1.80 (O_2C−CH_3)

Synthesis of ZnL^{2}I (3). Methyl iodide (57 μL, 0.909 mmol) was added to 50 mL of acetonitrile containing **1** (300 mg, 0. 909 mmol). The solution was refluxed for 24 h and then concentrated to approximately 5 mL under vacuum and placed in a freezer for 4 h. The resulting solid was filtered and washed with diethyl ether with a yield of 78% (333 mg, 0.709 mmol). X-ray quality crystals were obtained upon slow evaporation in air of 3 mM solution of **3** in a 1:1:1 mixture of acetone/methanol/acetonitrile. Anal. Calcd for $ZnC_{12}H_{17}N_6SI\cdot 3H_2O$: C, 27.50 H, 3.70; N, 15.86. Found: C, 27.56; H, 3.32; N, 15.61. Maldi-TOF MS: *m*/*z* calcd for $ZnSC_{12}N_6H_{17}\cdot CH_3CN$: 382. Found: 382.08. ^{1}H NMR (400 MHz, DMSO-d_6) δ/ppm: 8.10 (Ar−H), 8.04 (Ar−H), 7.86(*NH*−CH_3), 7.38 (Ar−H), 7.16 (Ar−H), 3.62 (N−CH_3), 2.90 (NH−CH_3), 2.33, 2.07(C−CH_3). ^{13}C NMR (400 MHz, DMSO-d_6) δ/ppm: 176.97 (C_1), 157.19 (C_4), 153.90 (C_8), 145.98, 145.52 (C_2, C_3), 141.96 (C_6), 140.15 (C_7), 111.69 (C_5), 41.71 (C_{12}), 29.55 (C_9) 17.34(C_{10}), 14.05 (C_{11}). IR (cm^{-1}): 3440, 2931, 1604, 1481, 1389, 1296, 1219, 1080, 817, 771, 679. UV/vis in methanol: 435 nm (ε = 2084 L mol^{-1} cm^{-1}), 315 nm (ε = 5038 L mol^{-1} cm^{-1}).

Crystallographic Studies. A thin yellow prism 0.27 × 0.08 × 0.06 mm^3 crystal of **2** grown from a solution of acetonitrile/methanol/acetone was mounted on a CryoLoop for collection of X-ray data on an Agilent Technologies/Oxford Diffraction Gemini CCD diffractometer. The CrysAlisPro[33] CCD software package (v 1.171.36.32) was used to acquire a total of 727 30-s frame ω-scan exposures of data at 100 K to a $2\theta_{max}$ = 54.12° using monochromated Mo Kα radiation (0.71073 Å) from a sealed tube. Frame data were processed using CrysAlisPro[33] RED to determine final unit cell parameters: a = 7.2770(3) Å, b = 7.6340(3) Å, c = 17.8924(7) Å, α = 91.102(3)°, β = 92.654(3)°, γ =115.763(4)°, V = 893.35(6) Å^3, D_{calc} = 1.442 Mg/m^3, Z = 2 to produce raw *hkl* data that were then corrected for absorption (transmission min./max. = 0.907/1.000; μ= 1.508 mm^{-1}) using SCALE3 ABSPACK.[34] The structure was solved by Direct methods in the space group $P\bar{1}$ using SHELXS[35] and refined by least-squares methods on F^2 using SHELXL.[35] Non-hydrogen atoms were refined with anisotropic atomic displacement parameters. Imine H's were located by difference maps and refined isotropically. Methyl hydrogen atoms were placed in their geometrically generated positions and refined as a riding model and these atoms were assigned $U(H) = 1.5 \times U_{eq}$. For all 3915 unique reflections (R(int) 0.037), the final anisotropic full matrix least-squares refinement on F^2 for 236 variables converged at R_1 = 0.033 and wR_2 = 0.075 with a GOF of 1.08.

A yellow prism 0.20 × 0.20 × 0.03 mm^3 crystal of **3** grown from a solution of acetonitrile/methanol/acetone was mounted on a glass fiber for collection of X-ray data on an Agilent Technologies/Oxford Diffraction Gemini CCD diffractometer. The CrysAlisPro[33] CCD software package (v 1.171.36.32) was used to acquire a total of 857 40-s frame ω-scan exposures of data at 100 K to a $2\theta_{max}$ = 60.20° using monochromated Mo Kα radiation (0.71073 Å) from a sealed tube. Frame data were processed using CrysAlisPro[33] RED to determine final unit cell parameters: a = 7.2994(3) Å, b = 12.8478(5) Å, c = 17.248(2) Å, α = 90.0°, β = 90.0°, γ = 90.0°, V = 1617.5(2) Å^3, D_{calc} = 1.929 Mg/m^3, Z = 4 to produce raw *hkl* data that were then corrected for absorption (transmission min./max. = 0.663/1.00; μ= 3.558 mm^{-1}) using SCALE3 ABSPACK.[34] The structure was solved by Direct methods in the orthorhombic space group $P\ 2_1\ 2_1\ 2_1$ using SHELXS[35] and refined by least-squares methods on F^2 using SHELXL.[35] Non-hydrogen atoms were refined with anisotropic atomic displacement parameters. Imine H's and pyridyl H's were located by difference maps and refined isotropically. Methyl hydrogen atoms were placed in their geometrically generated positions and refined as a riding model and these atoms were assigned $U(H) = 1.5 \times U_{eq}$. For all 4750 unique reflections (R(int) 0.041), the final anisotropic full matrix least-squares refinement on F^2 for 236 variables converged at R_1 = 0.029 and wR_2 = 0.056 with a GOF of 1.08.

Electrochemical Methods. All cyclic voltammetry (CV) and CPC measurements were recorded using a Gamry Interface potentiostat/galvanostat connected to a glassy carbon working electrode (3.0 mm diameter surface area = 0.07 cm^2), a platinum counter electrode, and Ag/Ag$^+$ reference electrode. Before use, the working electrode was polished using an aqueous alumina slurry. The working and counter electrode were rinsed with ethanol, acetone, DI water, and finally acetonitrile, then sonicated for 15 min in acetonitrile. CV experiments were conducted in a five-necked electrochemical cell. Three necks were used for each electrode. The other necks were used to maintain a constant Ar atmosphere during data acquisition and to introduce solids, acids, and solvent levels. Overpotential and turnover frequency calculations were performed as previously reported.[12]

CPC measurements were conducted to determine Faradaic efficiencies were performed using an H-tube fitted with a frit. The working compartment contained a glassy carbon and a Ag/Ag$^+$ reference electrode. The counter electrode compartment was fitted with a platinum wire. All CV and CPC measurements were performed using solutions containing 0.1 M Bu_4NPF_6 in acetonitrile and 1 mM **1** or **3**. In CPC studies, the H-tube was charged with 44 mL of 1 mM **1** or **3** in acetonitrile and 0.240 M acetic acid and purged with Ar for 15 min. The H-tube was then inverted, and CPC was conducted at −2.60 V vs Ag/AgCl for 2h. In the case of the control experiment for **2**, the concentration was 0.58 and 0.286 mM, respectively. Ferrocene was used as an internal standard, except during the concentration dependence studies and control experiments. Evolved gas from the cathode compartment displaced solvent in a cylinder with diameter 1.12 cm. Each volume of gas was then calculated via the volume of a cylinder, and then using the ideal gas law, a value for number of moles of hydrogen was determined. The amount of gas produced was subtracted from the gas produced via experiments sans catalyst, or the "blank" experiment. The total charge passed was also subtracted from the "blank" experiment, and from there, the theoretical moles of gas was determined (see the Supporting Information). From there, the faradaic efficiency equation was utilized to determine the faradaic efficiencies of each catalyst in each solvent.

To identify the gaseous product of electrocatalysis, CPC measurements were completed in a two-compartment electrolysis cell, that was fitted with a frit to separate the two compartments. The working compartment was charged with 1 mM **1** or **3**, 0.1 M NBu_4PF_6, and acid-saturating glacial acetic acid and filled with acetonitrile, with both the working electrode and reference electrode. The other compartment was charged with 0.1 M NBu_4PF_6 and acetonitrile with a platinum counter electrode. The CPC was carried out for 24 h, and the evolved gas was subjected to gas chromatography (GC-TCD) analysis at the end of electrolysis using a Gow-MAC series 400 GC-TCD equipped with a molecular sieve column for product detection. The column was heated to 130 °C under N_2 gas flow with 250 μL injection samples. Control studies of the CV and CPC experiments were done under the exact same conditions with the absence of 1 mM **1**, **2**, or **3**.

Catalysis Control Experiments. *Soak Test.* The glassy carbon electrode was immersed in a scintillation vial containing an acetonitrile solution of 1 mM of **1**, 0.1 M Bu_4NPF_6, and 0.240 M acetic acid for 24 h. The same conditions were applied to **3**, with the exception that 0.072 M acetic acid was used. The electrode was removed from the vial, and the outside edge was rinsed carefully with DI H_2O, taking care not to touch the working portion of the electrode. The rinsed electrode was immersed in a fresh solution of 0.1 M Bu_4NPF_6 in acetonitrile and CVs were recorded at scan rates of 0.2, 0.5, and 1.0 V/s.

Post-CV Dip Test. A polished glassy carbon electrode was immersed in an acetonitrile solution containing 1 mM **1** or **3**, 0.1 M Bu_4NPF_6, and enough acetic acid to reach acid-saturation conditions. The electrode was repeatedly cycled between −0.5 V and the ending catalysis potential (−3.4 V for **1** and −2.2 V for **3**) vs Fc$^+$/Fc for 10−30 cycles at a scan rate of 0.2 V/s. The electrodes were then removed from solution and rinsed carefully with DI H_2O. The rinsed electrode was immersed in a fresh solution of 0.1 M Bu_4NPF_6 in acetonitrile, and CVs were recorded at scan rates of 0.2, 0.5, and 1.0

V/s. Acetic acid was then added to obtain acid-saturating conditions, and the CVs were recollected.

Controlled Potential Coulometry Tests. The CPC tests for stability and electrode deposition were done in a two-compartment cell separated via a frit. One compartment housed a stir bar, 1 mM **1** or **3**, 0.1 M Bu_4NPF_6, and enough acetic acid to reach acid-saturation conditions in acetonitrile, as well as the working and reference electrodes. The other compartment held the Pt counter electrode and 0.1 M Bu_4NPF_6 in acetonitrile. The working compartment was purged with Ar for 15 min. The potential was then held at −2.60 V for **1** or −2.20 V for **3** for 24 h. The electrodes were then removed from solution, rinsed carefully with DI H_2O, and placed in a fresh solution of 0.1 M Bu_4NPF_6 in acetonitrile. CVs were recorded (see Supporting Information). Acid at saturating conditions was then added to these solutions, and CVs were also recorded. Samples for XPS analysis were collected by scraping material from the dried electrode surface.

Postelectrolysis Rinse Test. A CPC was done in the H-Cell as described above in the CPC test. After that CPC the electrode was removed, rinsed with DI H_2O, and placed into a fresh solution with 0.240 or 0.072 M acetic acid, 0.1 M NBu_4PF_6 in acetonitrile. A second CPC was conducted over 2 h.

XPS Experiments. The XPS experiments were carried out using a PHI *VersaProbe* II instrument equipped with a focused monochromatic Al K(alpha) source. The instrument base pressure was ca. 8×10^{-10} Torr. For all experiments, an X-ray power of 25 W at 15 kV was used with a 100 μm beam size at the X-ray incidence and take-off angles of 45°. Additional elemental mapping experiments were completed using a 20 μm beam size. The instrument work function was calibrated to give a binding energy (BE) of 84.0 eV for the Au $4f_{7/2}$ line for metallic gold and the spectrometer dispersion was adjusted to give a BE's of 284.8, 932.7, and of 368.3 eV for the C 1s line of adventitious (aliphatic) carbon presented on the nonsputtered samples, Cu $2p_{3/2}$ and Ag $3d_{5/2}$ photoemission lines, respectively. For all samples, the patented PHI dual charge neutralization system was used. High resolution I 3d, Zn 2p, and N 1s spectra were taken with a minimum of 10−60 s scans using 0.1 eV steps and 93.9 eV pass energy. The pass energy of 23.15 eV was used for C 1s. Signal above background measurement and Shirley background subtraction were carried out using MultiPak Version 9.3.0.3 PHI software. At the ultimate PHI *VersaProbe* II instrumental resolution, the temperature spread (at 14/86%) of the metallic silver Fermi edge was less than 120 meV. All XPS spectra were recorded using PHI software SmartSoft−VP Version 2.6.3.4 and processed using PHI MultiPack Version 9.3.0.3 and/or CasaXPS v.2.3.14. The relative sensitivity factors from MultiPack library were used to determine atomic percentages. Peaks were fitted using GL line shapes utilizing a combination of Gaussians and Lorentzians. Wherever possible, conclusions were drawn from the number of resolved signals for a given element, so as to minimize reliance on absolute binding energies for the nonconductive molecular materials. A given sample was examined at 5−6 different spots on the mounted specimen to ensure that consistent, reproducible results were obtained. The high resolution I $3d_{5/2}$ XPS spectra have been deconvoluted into two components, I_1 and I_2, generating reasonably good fits.

Resistance Measurements. Resistance measurements were conducted using a Metroham Autolab potentiostat. First, 0.5 mM solutions of **2**, **3**, tetrabutylammonium hexafluorophosphate, and *para*-nitroaniline were prepared. A 5 mL aliquot of each solution was placed in separate beakers between two graphite rods that were 2.5 cm apart. This was then subjected to resistance measurement experiment provided by the Nova software made by Metroham Autolab.

Titration Experiments. A series of 1 mM solutions (10 mL) of **1**, **2**, and **3** were prepared in acetonitrile. The solutions were then diluted to a 0.1 mM and titrated with a 0.1 M solution of acetic acid in acetonitrile. Titrations were monitored by UV−vis spectroscopy. After each addition, solutions were allowed to equilibrate for 3 minutes.

NMR Studies. In an NMR tube, 5 mg of **2** was dissolved in DMSO-d_6. To this solution was added 25 μL of HPF_6 (45 wt %) in water. The solution turned from red to yellow and displayed peaks at δ/ppm 11.58 (imido (N−H)), 10.30 (hydrazino N−H), 10.16 (hydrazino N−H), 8.45 (Ar−H), 8.33 (Ar−H), 8.08 (Ar−H), 7.45 (*NH*−CH_3), 7.13 (Ar−H), 3.15 (N−CH_3), 2.16 (C−CH_3) (6), 1.88 (O−C(O)−CH_3).

In an NMR tube, 5 mg of **3** was dissolved in DMSO-d_6. To this solution was added 25 μL of HPF_6 (45 wt %) in water. The solution turned from red to yellow and displayed peaks at δ/ppm 11.54 (imido (N−H)), 10.53 (hydrazino N−H), 10.24 (imido N−H), 8.45 (Ar−H), 8.08 (Ar−H), 7.97 (Ar−H), 7.42 (*NH*−CH_3), 7.33 (Ar−H), 3.12 (N−CH_3) (1proton), 3.00 (NH−CH_3), 2.76 (N−CH_3) (1proton), 2.66 (N−CH_3) (1proton), 2.26 (C−CH_3), 2.20 (C−CH_3).

Computational Methods. DFT was successfully employed to calculate and to validate the experimental observables. DFT is less expensive than other computational methods and can predict the energetics and the geometrical structures of a model system with a considerable accuracy. The accuracy of the DFT is largely dependent on the choice of a proper functional. On the basis of our previous studies of related complexes, it was shown that the B3LYP, a hybrid functional can produce reliable agreement with experimental parameters such as bond lengths, bond angles, and torsional angles.[17] In this regard, we have applied B3LYP functional to optimize the structures with 6-311g(d,p) basis set.[25,26] This level of theory was also applied in our previous studies and found to be quite accurate. The calculations were conducted in a polarizable continuum model (PCM).[27] Acetonitrile was used as a solvent in PCM as this has been used in our experiment. The optimized structures were confirmed by frequency calculations. No imaginary frequencies were found for the optimized geometries which confirms the optimized structure were true stationery points. All corresponding Cartesian coordinates were added in the Supporting Information. Gaussian 09 was used to conduct the calculations.[36] Chemcraft and gaussview were used to visualize the structures.[37]

■ ASSOCIATED CONTENT

Supporting Information

The Supporting Information is available free of charge on the ACS Publications website at DOI: 10.1021/acs.inorgchem.9b01912.

Sample calculations, crystallographic details, NMR, IR, and UV/vis spectra, additional electrochemical data, high resolution XPS spectra, additional computational analysis, and computation input coordinates (PDF)

Cartesian coordinates (PDF)

Accession Codes

CCDC 1921210 and 1921211 contain the supplementary crystallographic data for this paper. These data can be obtained free of charge via www.ccdc.cam.ac.uk/data_request/cif, or by emailing data_request@ccdc.cam.ac.uk, or by contacting The Cambridge Crystallographic Data Centre, 12 Union Road, Cambridge CB2 1EZ, UK; fax: +44 1223 336033.

■ AUTHOR INFORMATION

Corresponding Author

*E-mail: craig.grapperhaus@louisville.edu.

ORCID

Steve P. Cronin: 0000-0001-6328-706X
Abdullah Al Mamun: 0000-0001-8941-8195
Megan J. Toda: 0000-0002-4913-0848
Pawel M. Kozlowski: 0000-0002-4090-8078
Craig A. Grapperhaus: 0000-0003-4889-2645

Notes

The authors declare no competing financial interest.

■ ACKNOWLEDGMENTS

This research was supported in part by the National Science Foundation CHE-1665136 (C.A.G.) and CHE-1800245 (R.M.B.). M.S.M. thanks the Department of Energy (DEFG02-08CH11538) and the Kentucky Research Challenge Trust Fund for upgrade of our X-ray facilities. The XPS instrument at the IU Bloomington was funded by the NSF DMR MRI-1126394.

■ REFERENCES

(1) Gray, H. B. Powering the planet with solar fuel. *Nat. Chem.* **2009**, *1*, 7.

(2) Cook, T. R.; Dogutan, D. K.; Reece, S. Y.; Surendranath, Y.; Teets, T. S.; Nocera, D. G. Solar energy supply and storage for the legacy and nonlegacy worlds. *Chem. Rev.* **2010**, *110*, 6474−502.

(3) Lewis, N. S.; Nocera, D. G. Powering the planet: Chemical challenges in solar energy utilization. *Proc. Natl. Acad. Sci. U. S. A.* **2006**, *103*, 15729.

(4) Grutza, M.-L.; Rajagopal, A.; Streb, C.; Kurz, P. Hydrogen evolution catalysis by molybdenum sulfides (MoSx): are thiomolybdate clusters like [Mo3S13]2− suitable active site models? *Sustain. Energy Fuels* **2018**, *2*, 1893−1904.

(5) Garrett, B. R.; Polen, S. M.; Pimplikar, M.; Hadad, C. M.; Wu, Y. Anion-Redox Mechanism of $MoO(S_2)_2$(2,2′-bipyridine) for Electrocatalytic Hydrogen Production. *J. Am. Chem. Soc.* **2017**, *139*, 4342−4345.

(6) Karunadasa, H. I.; Montalvo, E.; Sun, Y.; Majda, M.; Long, J. R.; Chang, C. J. A Molecular MoS_2 Edge Site Mimic for Catalytic Hydrogen Generation. *Science* **2012**, *335*, 698.

(7) Helm, M. L.; Stewart, M. P.; Bullock, R. M.; DuBois, M. R.; DuBois, D. L. A Synthetic Nickel Electrocatalyst with a Turnover Frequency Above 100,000 s^{-1} for H_2 Production. *Science* **2011**, *333*, 863.

(8) Graziono, G. Homogeneous catalysis: An electrochemical and spectroscopic look at renewable energy. *Nat. Rev. Chem.* **2018**, *2*, 0130.

(9) Haddad, A. Z.; Kumar, D.; Ouch Sampson, K.; Matzner, A. M.; Mashuta, M. S.; Grapperhaus, C. A. Proposed Ligand-Centered Electrocatalytic Hydrogen Evolution and Hydrogen Oxidation at a Noninnocent Mononuclear Metal−Thiolate. *J. Am. Chem. Soc.* **2015**, *137*, 9238−9241.

(10) Thompson, E. J.; Berben, L. A. Electrocatalytic Hydrogen Production by an Aluminum(III) Complex: Ligand-Based Proton and Electron Transfer. *Angew. Chem., Int. Ed.* **2015**, *54*, 11642−11646.

(11) Haddad, A. Z.; Garabato, B. D.; Kozlowski, P. M.; Buchanan, R. M.; Grapperhaus, C. A. Beyond Metal-Hydrides: Non-Transition-Metal and Metal-Free Ligand-Centered Electrocatalytic Hydrogen Evolution and Hydrogen Oxidation. *J. Am. Chem. Soc.* **2016**, *138*, 7844−7847.

(12) Haddad, A. Z.; Cronin, S. P.; Mashuta, M. S.; Buchanan, R. M.; Grapperhaus, C. A. Metal-Assisted Ligand-Centered Electrocatalytic Hydrogen Evolution upon Reduction of a Bis(thiosemicarbazonato)-Cu(II) Complex. *Inorg. Chem.* **2017**, *56*, 11254−11265.

(13) Jain, R.; Mamun, A. A.; Buchanan, R. M.; Kozlowski, P. M.; Grapperhaus, C. A. Ligand-Assisted Metal-Centered Electrocatalytic Hydrogen Evolution upon Reduction of a Bis(thiosemicarbazonato)-Ni(II) Complex. *Inorg. Chem.* **2018**, *57*, 13486−13493.

(14) Straistari, T.; Fize, J.; Shova, S.; Réglier, M.; Artero, V.; Orio, M. A Thiosemicarbazone−Nickel(II) Complex as Efficient Electrocatalyst for Hydrogen Evolution. *ChemCatChem* **2017**, *9*, 2262−2268.

(15) Straistari, T.; Hardré, R.; Massin, J.; Attolini, M.; Faure, B.; Giorgi, M.; Réglier, M.; Orio, M. Influence of the Metal Ion on the Electrocatalytic Hydrogen Production by a Thiosemicarbazone Palladium Complex. *Eur. J. Inorg. Chem.* **2018**, *2018*, 2259−2266.

(16) Wise, C. F.; Liu, D.; Mayer, K. J.; Crossland, P. M.; Hartley, C. L.; McNamara, W. R. A nickel complex of a conjugated bis-dithiocarbazate Schiff base for the photocatalytic production of hydrogen. *Dalton Trans.* **2015**, *44*, 14265−14271.

(17) Cowley, A. R.; Dilworth, J. R.; Donnelly, P. S.; White, J. M. Copper Complexes of Thiosemicarbazone−Pyridylhydrazine (THYNIC) Hybrid Ligands: A New Versatile Potential Bifunctional Chelator for Copper Radiopharmaceuticals. *Inorg. Chem.* **2006**, *45*, 496−498.

(18) Calatayud, D. G.; López-Torres, E.; Dilworth, J. R.; Antonia Mendiola, M. Complexes of group 12 metals containing a hybrid thiosemicarbazone-pyridylhydrazone ligand. *Inorg. Chim. Acta* **2012**, *381*, 150−161.

(19) Farrugia, L. J. ORTEP-3 for Windows. *J. Appl. Crystallogr.* **1997**, *30*, 565.

(20) Bentley, C. L.; Bond, A. M.; Hollenkamp, A. F.; Mahon, P. J.; Zhang, J. Voltammetric Determination of the Iodide/Iodine Formal Potential and Triiodide Stability Constant in Conventional and Ionic Liquid Media. *J. Phys. Chem. C* **2015**, *119*, 22392−22403.

(21) Fourmond, V.; Jacques, P.-A.; Fontecave, M.; Artero, V. H_2 Evolution and Molecular Electrocatalysts: Determination of Overpotentials and Effect of Homoconjugation. *Inorg. Chem.* **2010**, *49*, 10338−10347.

(22) Costentin, C.; Drouet, S.; Robert, M.; Savéant, J.-M. Turnover Numbers, Turnover Frequencies, and Overpotential in Molecular Catalysis of Electrochemical Reactions. Cyclic Voltammetry and Preparative-Scale Electrolysis. *J. Am. Chem. Soc.* **2012**, *134*, 11235−11242.

(23) McCarthy, B. D.; Martin, D. J.; Rountree, E. S.; Ullman, A. C.; Dempsey, J. L. Electrochemical Reduction of Brønsted Acids by Glassy Carbon in Acetonitrile—Implications for Electrocatalytic Hydrogen Evolution. *Inorg. Chem.* **2014**, *53*, 8350−8361.

(24) Gupta, A. J.; Vishnosky, N. S.; Hietsoi, O.; Losovyj, Y.; Strain, J.; Spurgeon, J.; Mashuta, M. S.; Jain, R.; Buchanan, R. M.; Gupta, G.; Grapperhaus, C. A. Effect of Stacking Interactions on the Translation of Structurally Related Bis-thiosemicarbazone Ni(II) HER Catalysts to Modified Electrode Surfaces. *Inorg. Chem.* **2019**, DOI: 10.1021/acs.inorgchem.9b01209.

(25) Lee, C.; Yang, W.; Parr, R. G. Development of the Colle-Salvetti correlation-energy formula into a functional of the electron density. *Phys. Rev. B: Condens. Matter Mater. Phys.* **1988**, *37*, 785−789.

(26) Wong, M. W.; Gill, P. M. W.; Nobes, R. H.; Radom, L. 6-311G(MC)(d,p): a second-row analogue of the 6-311G(d,p) basis set: calculated heats of formation for second-row hydrides. *J. Phys. Chem.* **1988**, *92*, 4875.

(27) Scalmani, G.; Frisch, M. J. Continuous surface charge polarizable continuum models of solvation. I. General formalism. *J. Chem. Phys.* **2010**, *132*, 114110.

(28) Ding, S.; Ghosh, P.; Darensbourg, M. Y.; Hall, M. B. Interplay of hemilability and redox activity in models of hydrogenase active sites. *Proc. Natl. Acad. Sci. U. S. A.* **2017**, *114*, E9775.

(29) Marenich, A. V.; Ho, J.; Coote, M. L.; Cramer, C. J.; Truhlar, D. G. Computational electrochemistry: prediction of liquid-phase reduction potentials. *Phys. Chem. Chem. Phys.* **2014**, *16*, 15068−15106.

(30) Ngo, K. T.; McKinnon, M.; Mahanti, B.; Narayanan, R.; Grills, D. C.; Ertem, M. Z.; Rochford, J. Turning on the Protonation-First Pathway for Electrocatalytic CO_2 Reduction by Manganese Bipyridyl Tricarbonyl Complexes. *J. Am. Chem. Soc.* **2017**, *139*, 2604−2618.

(31) Lee, K. J.; Elgrishi, N.; Kandemir, B.; Dempsey, J. L. Electrochemical and spectroscopic methods for evaluating molecular electrocatalysts. *Nat. Rev. Chem.* **2017**, *1*, 0039.

(32) Roubelakis, M. M.; Bediako, D. K.; Dogutan, D. K.; Nocera, D. G. Proton-coupled electron transfer kinetics for the hydrogen evolution reaction of hangman porphyrins. *Energy Environ. Sci.* **2012**, *5*, 7737−7740.

(33) *CrysAlis Pro (CCD and RED)*; Aligent, 2013.

(34) SCALE3 ABSPACK. In *CrysAlis Pro (RED)*; Aligent, 2013.

(35) Sheldrick, G. M. A short history of SHELX. *Acta Crystallogr., Sect. A: Found. Crystallogr.* **2008**, *A64*, 112−122.

(36) Frisch, M. J.; Trucks, G. W.; Schlegel, H. B.; Scuseria, G. E.; Robb, M. A.; Cheeseman, J. R.; Scalmani, G.; Barone, V.; Petersson, G. A.; Nakatsuji, H.; Li, X.; Caricato, M.; Marenich, A. V.; Bloino, J.;

Janesko, B. G.; Gomperts, R.; Mennucci, B.; Hratchian, H. P.; Ortiz, J. V.; Izmaylov, A. F.; Sonnenberg, J. L.; Williams-Young, D.; Ding, F.; Lipparini, F.; Egidi, F.; Goings, J.; Peng, B.; Petrone, A.; Henderson, T.; Ranasinghe, D.; Zakrzewski, V. G.; Gao, J.; Rega, N.; Zheng, G.; Liang, W.; Hada, M.; Ehara, M.; Toyota, K.; Fukuda, R.; Hasegawa, J.; Ishida, M.; Nakajima, T.; Honda, Y.; Kitao, O.; Nakai, H.; Vreven, T.; Throssell, K.; Montgomery, J. A., Jr.; Peralta, J. E.; Ogliaro, F.; Bearpark, M.; Heyd, J. J.; Brothers, E. N.; Kudin, K. N.; Staroverov, V. N.; Kobayashi, R.; Normand, J.; Raghavachari, K.; Rendell, A.; Burant, J. C.; Iyengar, S. S.; Tomasi, J.; Cossi, M.; Millam, J. M.; Klene, M.; Adamo, C.; Cammi, R.; Ochterski, J. W.; Martin, R. L.; Morokuma, K.; Farkas, O.; Foresman, J. B.; Fox, D. J. *Gaussian 16*, revision B.01; Gaussian, Inc.: Wallingford CT, 2016.

(37) *Chemcraft - graphical software for visualization of quantum chemistry computations*. https://www.chemcraftprog.com.